Precision Engineering 35 (2011) 248–257

Contents lists available at ScienceDirect

Precision Engineering

journal homepage: www.elsevier.com/locate/precision

An interferometric platform for studying AFM probe deflection

Lee Kumanchik [a], Tony L. Schmitz [a,*], Jon R. Pratt [b]

[a] Department of Mechanical and Aerospace Engineering, University of Florida, Gainesville, FL 32611, United States
[b] Manufacturing Engineering Laboratory, National Institute of Standards and Technology, Gaithersburg, MD 20899, United States

ARTICLE INFO

Article history:
Received 29 October 2009
Received in revised form 30 August 2010
Accepted 23 September 2010

Keywords:
Atomic force microscope
Cantilever
Beam
Deflection

ABSTRACT

This paper describes an interferometric platform for measuring the full-field deflection of atomic force microscope (AFM) probes and generic cantilevers during quasi-static loading. The platform consists of a scanning white light interferometer (SWLI), holders for the cantilevers, a translation stage, a rotation (tip-tilt) stage, and an adapter plate to connect these items to the SWLI table. Visualization of cantilever bending behavior is demonstrated for snap-in against a rigid surface, cantilever-on-cantilever tests, and a damaged AFM probe. A new approach to normal force calculation using a polynomial fit to the cantilever deflection profile is also presented and verified experimentally. The method requires only the coefficient for the third order (cubic) term from the fit to the deflection profile, the elastic modulus, and the area moment of inertia for the cantilever under test.

1. Introduction

Since its development in 1986 by Binnig et al. [1], the atomic force microscope (AFM) has played a major role in the advancement of nanotechnology. Current AFM applications include, for example: (1) small force measurement, supporting various disciplines such as biotechnology and nanotribology; (2) imaging of such disparate surfaces as biomolecules and Martian soil [2]; (3) various physical, chemical, and biological sensors (trace gas/vapor detection) [3]; and (4) and data storage/retrieval [4].

Because the AFM has become an important instrument for small force measurement, defining the relationship between probe deflection and probe–surface interaction forces is an international research priority. Traditionally, this relationship is treated as a scalar "spring stiffness" which relates vertical load[1] to probe displacement, usually determined using an optical scheme where a laser beam is reflected off the probe backside onto a position sensitive photodetector. As noted by Cumpson et al. [5], four basic approaches have been evaluated (e.g., [6–19]):

- a comparison of the test probe to a reference cantilever of known stiffness;
- calibration against the energy of thermal vibrations;
- the addition of known particle masses; and
- a combination of resonant frequency measurements with the test probe's dimensions and material properties.

Each approach has its own difficulties and accuracy limitations. These are summarized in Refs. [5,16], for example. Some of the obstacles associated with these methods include: accurately positioning the test probe tip on the reference cantilever (the stiffness value is dependent on the position along the cantilever); partitioning acoustic and mechanical noise in thermal vibrations analysis; and accurately and efficiently placing small masses on the test cantilever.

While the stiffness calibration for vertical force imposes significant difficulties in itself, the probe–surface interaction forces in practice are not limited to a single vertical force. Naturally, a lateral force is also developed due to friction between the probe and surface during relative translation. To quantify the lateral force, the "spring stiffness" approach is again generally adopted, but now the relationship between rotation of the probe (about its axis during translation perpendicular to its axis) and the friction force is developed. A popular approach for obtaining this spring constant is the "wedge" method proposed by Ogletree et al. [20] which takes advantage of the known facet angle for the $SrTiO_3$ (3 0 5) surface. While others methods have also been investigated (e.g., [21–23]), a primary limiting factor is often the required vertical force spring constant.

To address government and industry needs in AFM force measurement, the National Institute of Standards and Technology supports the Small Force Metrology project within the Manufacturing Metrology Division's Mass and Force Group. This project studies

* Corresponding author. Tel.: +1 352 392 8909; fax: +1 352 392 1071.
E-mail address: tschmitz@ufl.edu (T.L. Schmitz).
[1] A horizontal or slightly angled probe is assumed.

0141-6359/$ – see front matter © 2010 Elsevier Inc. All rights reserved.
doi:10.1016/j.precisioneng.2010.09.013

force measurement in the piconewton (pN) to millinewton (mN) range and focuses on International System of Units (SI) traceability, including the development and testing of internationally accepted primary and secondary standards of force [24].

Historically, the Newton has been defined in terms of mass using subdivisions of a kilogram artifact traceable to the International Prototype Kilogram (e.g., the K20 prototype kilogram in the US) [25]. This imposes a limitation on the range of force magnitudes that can be traceably calibrated due to uncertainty levels for small subdivisions of the kilogram. To extend the force range below this magnitude [26,27], the Small Force Metrology project has developed the electrostatic force balance (EFB). This measurement platform enables lower uncertainty by deriving force in terms of voltage and capacitance instead of mass. Through comparisons of force measurements at the lower range of mass loading to the upper range of the EFB, it has been demonstrated that the EFB can achieve the accuracy required of a primary force standard.

Complementary efforts include moving from force realization to force dissemination [28] using secondary force artifacts. Due to the needs of the AFM community, the trend for these artifacts has been toward cantilever-based designs. The methodology has been to calibrate an artifact cantilever's stiffness by applying known forces with the EFB while measuring displacement. The calibrated force magnitude range can be increased by fabricating multiple cantilevers of varying stiffness [29] or calibrating the variable stiffness along the length of a single cantilever [30]. Additionally, experiments have shown the feasibility of a direct force transfer to piezoresistive and piezoelectric cantilevers [30,31]. The self-sensing nature of these cantilevers enables a force–voltage relation to be established directly. The only requirement for subsequent force measurements by a calibrated "piezo-lever" is to use a traceably calibrated voltmeter.

In support of these ongoing activities, an interferometric platform for measuring the full-field deflection of AFM probes and generic cantilevers during quasi-static loading was developed and is detailed here. The paper is organized as follows. Section 2 provides an opto-mechanical description of the platform. Section 3 includes imaging examples of various AFM probes under different loading scenarios. Section 4 describes an alternative method to calculating the vertical force applied to a cantilever; the new method uses the full deflection bending profile made available by the measurement platform. Conclusions are presented in Section 5.

2. Interferometric platform description

The purpose of the platform is to enable an AFM cantilever to be loaded against a sample[2] while measuring the full-field displacement of the cantilever. The setup consists of a scanning white light interferometer (SWLI), holders for the cantilevers, a translation stage, a rotation (tip-tilt) stage, and an adapter plate to connect these units to the SWLI table; see Fig. 1.

2.1. SWLI measurement

A key platform component is the SWLI, an optical three-dimensional surface profiler that uses interference of a broad spectrum light source, or "white light", to measure surface topography; see Fig. 2. Light reflected from the sample interferes with light reflected from a reference surface, but, unlike coherent source interference, the white light interference only occurs over a small optical path difference. By translating the objective (which carries the reference surface) relative to the test surface, a plot of the interference intensity for this path difference range can be captured on a pixel-by-pixel basis by the SWLI detector. The location of the modulated intensity (due to alternating constructive/destructive interference) region indicates the relative height of the sample at that pixel. Each pixel on the detector corresponds to a lateral position on the sample; the field of view for the corresponding height map depends on the system magnification. A Zygo NewView 7200[3] was used in this research. The selected system included a motorized translation/rotation (or X/Y/tip/tilt) table for sample alignment to the optical axis. As shown in Fig. 1, the platform is mounted on this table.

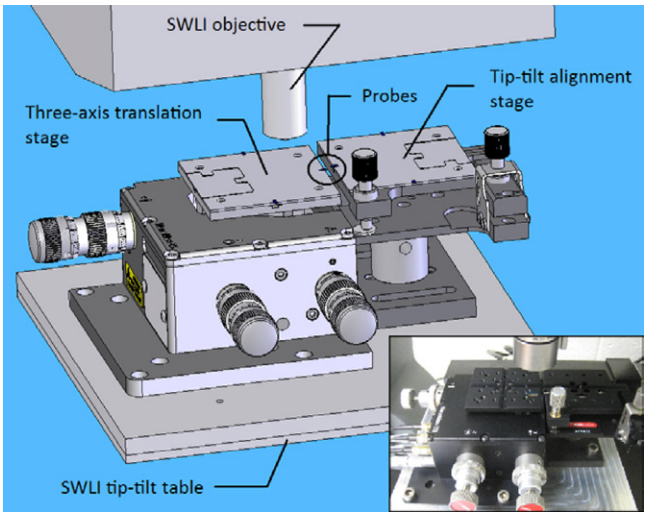

Fig. 1. The platform is composed of the SWLI, a translational stage, and a tip-tilt stage, which enables quasi-static cantilever-on-cantilever and cantilever-on-surface experiments to be conducted while measuring the full-field cantilever displacement.

There are different constraints associated with SWLI measurements relative to the traditional AFM optical scheme (where laser light is reflected from a single point on the backside of the probe to a photosensitive detector). First, a full height map may take up to several seconds to acquire, in general, since the objective must be translated. During this time the sample dynamics must be interrupted (the pseudo-static approach applied here) or synchronized with the measurement (the strobing approach – not used here). Second, the lateral resolution is typically orders of magnitude coarser than the vertical resolution along the optical axis. This is important because it is desired to view as much of the cantilever as possible to make the best use of the available pixels on the camera. For the experiments reported here, two objectives were used: a 5× Michelson with a lateral resolution of 2.2 μm/pixel and a 20× Mirau with a 0.55 μm/pixel lateral resolution (1× zoom and 640 × 480 pixel detector). In comparison, the NewView 7200 literature specifies a vertical resolution of 0.1 nm, although this value is dependent on the noise floor imposed by the measurement environment. Therefore, tests were performed to determine the repeatability for the experimental setup. A smooth silicon surface was placed on the stage at the cantilever loading location and 130 scans were completed using a 40 μm vertical scan range. The height repeatability for each pixel was then assessed. It was found that, on average,

[2] The sample may also be another cantilever, which can be the case for some calibration scenarios.

[3] Certain commercial equipment, instruments, or materials are identified in this article to adequately specify the experimental procedure. Such identification does not imply recommendation or endorsement by the National Institute of Standards and Technology, nor does it imply that the materials or equipment identified is necessarily the best available for the purpose.

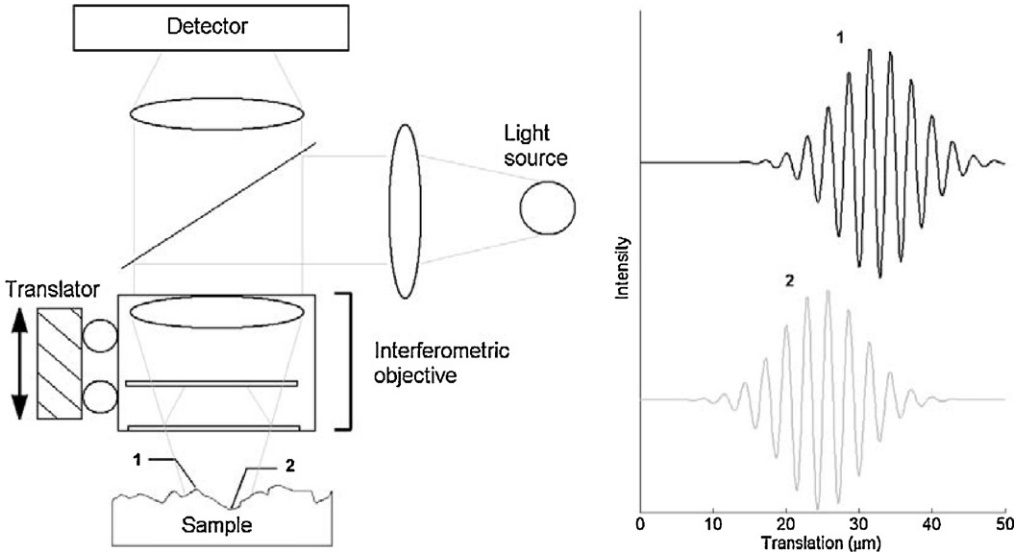

Fig. 2. SWLI schematic. A Mirau objective is represented, although other types are available. The left-to-right offset between the interference intensity from positions 1 and 2 indicates their relative height difference (positive translation in the upward direction).

each pixel reported the same position within a standard deviation of 2.7 nm. Therefore, a repeatability of 2.7 nm was assumed. Third, the SWLI cannot detect large height changes between adjacent points, so there is a maximum slope that can be detected. This slope varies depending on the selected objective/zoom; it was 4° for the 5× objective and 18° for the 20× objective (each at 1× zoom). For typical cantilever bending profiles, even the 4° slope limit is sufficient.

2.2. Cantilever holders

Aluminum plates with dimensions of 60 mm × 60 mm × 3 mm were fixed to the stages; see Fig. 3. Cantilevers and test surfaces were adhered to the plates at the midpoint of three sides (a fourth side with a specialized geometry was also available to enable cantilever alignment in future work). This design allowed the holder to be unscrewed and rotated to select the next cantilever for experimentation while approximately maintaining the same position in the SWLI field of view. A similar configuration was used for tests with a cantilever contacting a rigid surface. Cantilevers and rigid surfaces were bonded to the holders with adhesive to enable the required top-down view for the SWLI measurements.

2.3. Stages

The positioning stage (Thorlabs MAX301) was a three-axis, parallel kinematics, flexure-based design with 4 mm of coarse motion (thumbscrew actuation) and 20 μm of fine motion driven by piezoelectric actuators with strain gauge feedback. The motion was controlled by a Thorlabs BPC103 controller. The second stage was a manual tip-tilt platform (Thorlabs ATP002) positioned on a base assembly (Thorlabs AMA501) which enabled equal height, side-by-side use with the positioning stage. The tip-tilt platform provided ±4° of roll and pitch and acted as the fixed stage in the experiments. Any cantilever on this stage could be tilted into alignment with the positioning stage and then held fixed for the duration of the experiment.

2.4. Platform assembly

The platform assembly rested on the SWLI's motorized table. During use, the platform positioning stage was first aligned to the SWLI optical axis using the table. Then, the tip-tilt stage was aligned to the positioning stage. Since the SWLI angular detection limit can be low (depending on the objective and effective magnification),

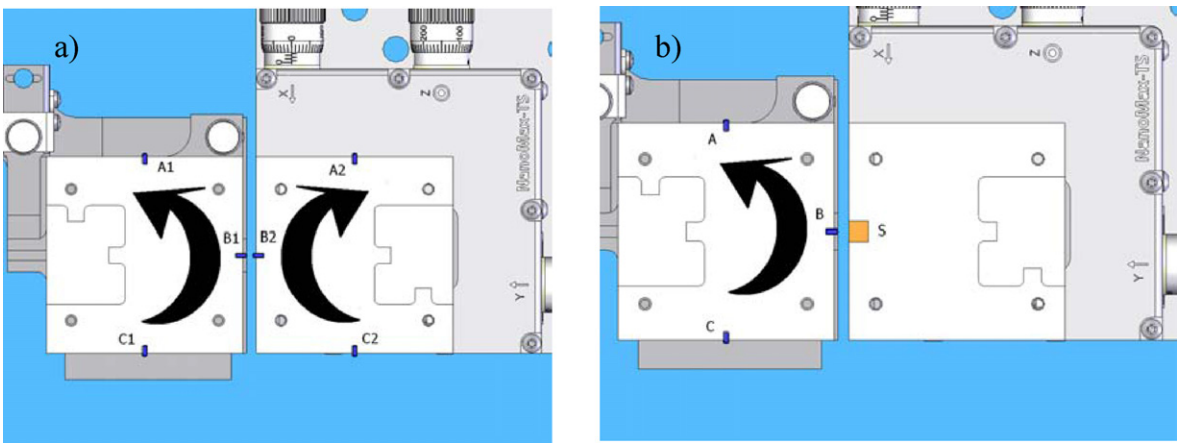

Fig. 3. Example cantilever placement on the aluminum holders (top views). The individual cantilevers are too small to be seen at this scale, but the monolithic base chips are labeled A1–C2 (a), A–C (b), and a rigid sample is labeled S (b). If the holders were unscrewed and rotated in the indicated direction, the next experiment would be C1 against C2 (a) and C against S (b).

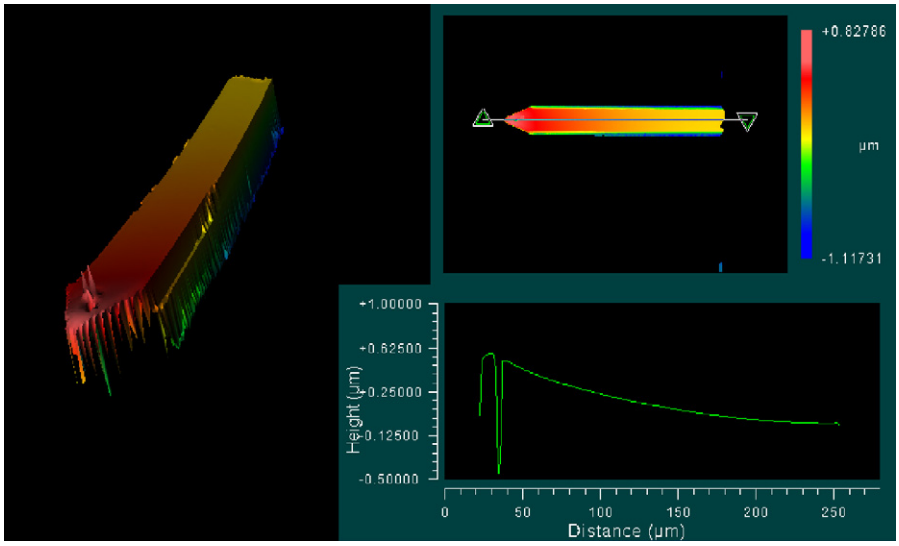

Fig. 4. The Olympus OMCL-AC240TS cantilever has a deformed shape causing ~0.5 µm of initial tip deflection.

proper alignment is important to maximize the available measurement range. Additionally, aligning to the optical axis ensures that vertical motion from the positioning stage produces no lateral motion in the field of view.

3. Visualization of quasi-static bending behavior

The interferometric platform enables the direct visualization of cantilever deformations without the need for interpretation via a single point measurement of cantilever tip motion used in conjunction with beam models. In this section deformed cantilever measurements are provided and primary imaging limitations are discussed [32].

3.1. Residual stress, "batwings", and differencing

The cantilevers presented here had a non-planar shape even in the absence of an external load. Cantilevers are typically designed to be flat, but residual stresses from the surface coating often lead to unwanted deformation. This deformation is typically small, but is observable in the SWLI measurements; see Fig. 4. This image displays the reflective backside of an Olympus OMCL-AC240TS (1.8 N/m stiffness) cantilever, where the laser would normally be positioned in an AFM. It is seen that the cantilever deformation is approximately 0.5 µm at the tip with no external load applied. An imaging artifact sometimes referred to as "batwings" is also observed. These spikes along the periphery of the cantilever are false height readings and tend to occur at steep height transitions. The speck near the tip (also visible in the section view) is surface contamination and also causes the bat wing effect. Additional cantilevers measurements are shown in Fig. 5. The data were collected using a 20× objective at 1× zoom in the 320 × 240 pixel mode.

When studying the deformation of beams it is necessary to separate the contributions due to the external load(s) from those caused by other sources, such as residual stress. For linear elastic beam models, deformation follows the rule of superposition. Therefore, in each of the analysis results presented here, the cantilever was measured before applying external loads. This reference image was then subtracted from all subsequent images to isolate the relative deformation caused by external loading. This differencing does not remove the batwings, however, as these locations tend to report random erroneous heights from image to image.

3.2. Snap-in

When an AFM cantilever is placed in close proximity to a surface, an attractive force develops which pulls the tip closer to the surface. At a critical gap size, the attractive force overcomes the cantilever's restorative elastic force and the tip snaps into contact with the surface. This attractive force represents one of the many load condi-

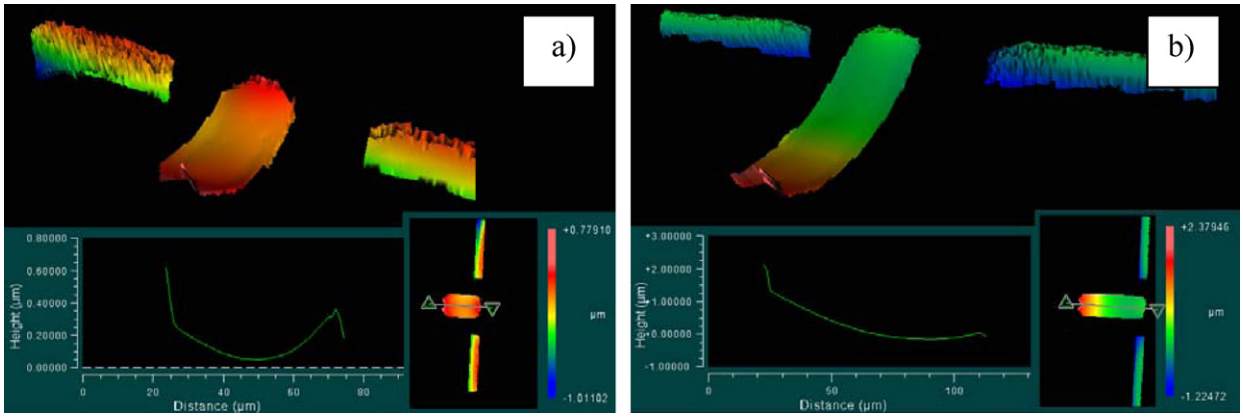

Fig. 5. Olympus cantilevers BL-RC150VB A with 0.03 N/m stiffness (a) and B with 0.006 N/m stiffness (b). The deformation levels are ~0.25 µm (a) and ~1 µm (b) in the absence of external loads.

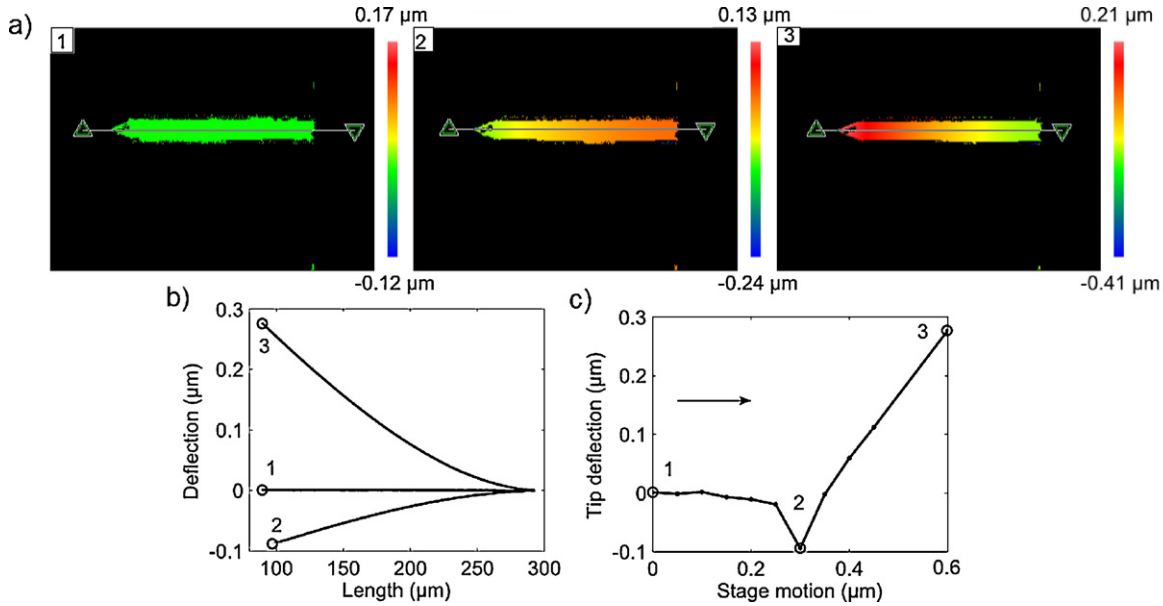

Fig. 6. Cantilever snap-in demonstration. (a) Height map of the cantilever at various stage locations, 1–3; (b) corresponding two-dimensional profiles, 1–3; and (c) traditional plot of stage motion versus tip deflection with 1–3 labeled. The arrow indicates the sequence of commanded stage motion.

tions AFM cantilevers experience. Snap-in behavior was measured for an Olympus OMCL-AC240TS (1.8 N/m) cantilever positioned near a smooth silicon surface; see Fig. 6. For these measurements, the silicon surface was mounted on the three-axis positioning stage and moved toward the cantilever in 50 nm steps. The sequence of three plots included in Fig. 6a displays the cantilever deformation profile for three stage locations. In position 1, the silicon surface is sufficiently far from the cantilever so that no appreciable attractive force is present. In position 2, snap-in has occurred. The cantilever deflection is approximately 0.1 μm at the tip. In position 3, the stage has continued to move vertically past the cantilever's undeformed position so that it is deflected upwards. In Fig. 6b, the centerline cantilever profiles are provided for the same three stage locations. The tip deflection versus stage motion is provided in Fig. 6c; measurement points are identified by the small circles in 50 nm increments and the three locations from Fig. 6a and b are represented by the large circles. Note that the information in this plot is all that is available from standard AFM single point deflection metrology. All images were captured using a 20× objective at 1× zoom in 320 × 240 pixel mode. The SWLI data was differenced to isolate the deformation caused by snap-in and it was filtered to remove the bat wing artifacts.

3.3. Other cantilever experiments

One of the benefits of full-field imaging is the ability to capture the height maps of the cantilever and sample simultaneously. For example, in cantilever-on-cantilever experiments using an AFM, measurements can only be made for the instrumented cantilever leaving the deflection of the other cantilever to be inferred. Using the interferometric platform, both cantilevers can be viewed simultaneously; see Fig. 7. This figure shows two Veeco 1930-00 (1.3 N/m, 35 μm wide) cantilevers with one cantilever pushing against the tip of the other. There is ∼9 μm of vertical offset between their bases and both cantilevers exhibit ∼4.5 μm of end deflection. The objective used was 20×, 0.8× zoom, in 640 × 480 pixel mode.

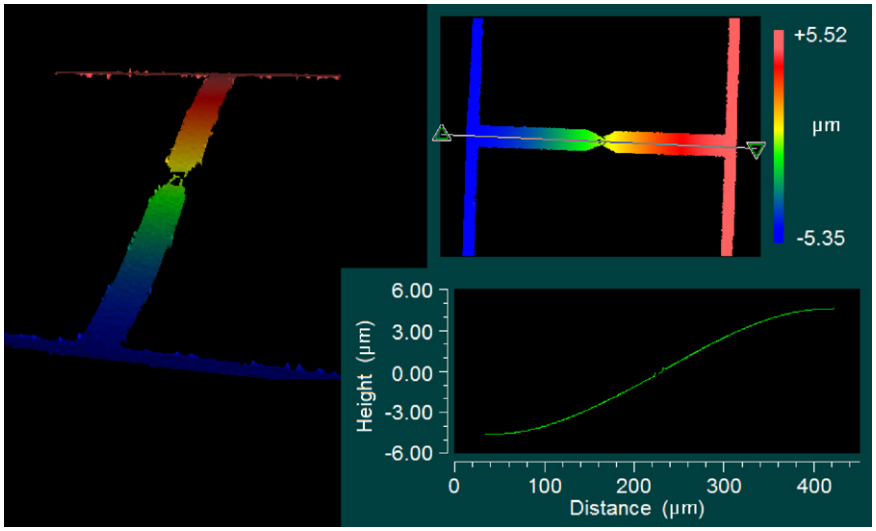

Fig. 7. Two Veeco 1930 (1.3 N/m, 35 μm wide) cantilevers in contact. The left cantilever lever tip is positioned above the right cantilever lever tip.

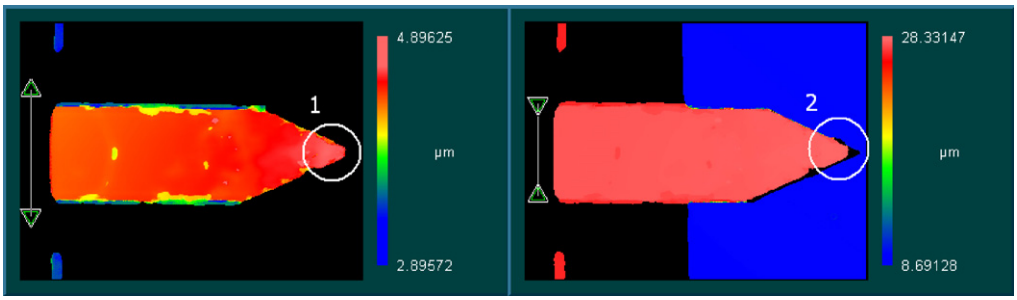

Fig. 8. Due to SWLI measurement limitations, data dropout is common on the cantilever periphery as is seen in area 1 (left image). This results in errors when determining the plan view dimensions. Including the sample in the measurement reveals lost data as is seen in area 2 (right image).

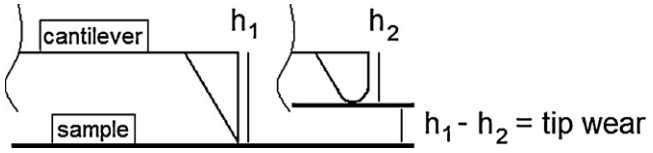

Fig. 9. Tip wear can be estimated using a SWLI measurement that includes the sample surface in the view. From an initial measurement, h1, to a current measurement, h2, the tip wear is h1–h2.

The sample can also be used as an aid in SWLI measurements of a cantilever's plan view dimensions. Due to SWLI measurement limitations, data dropout is common at the cantilever periphery. However, by placing a smooth sample underneath the cantilever as a backdrop, the lost pixels can be revealed; see Fig. 8. Additionally, the sample can aid in tip wear analysis. Though not demonstrated here, it is feasible to measure the distance from the sample to the surface of the cantilever to estimate progressive tip wear as depicted in Fig. 9.

Finally, an example of the platform's capability to identify anomalous bending behavior is presented in Fig. 10. Here, an Olympus OMCL-AC160TS (42 N/m) cantilever was pressed against a smooth silicon surface. The deflection profile was linear, rather than the expected cubic behavior. It is assumed that a crack at the cantilever base caused this hinge-like bending behavior. The cantilever broke off the base chip before this could be confirmed, but the fracture location supports the crack assumption. The imaging parameters included a 20× objective, 1× zoom, and 320 × 240 pixel mode.

4. Normal force calculation using polynomial fit

4.1. Single point deflection measurement

The current paradigm in relating cantilever deflection, y, to the probe force, F, is to apply Hooke's law, $F = ky$, where k is a scalar, calibrated stiffness constant and y is measured at a single point along the cantilever length. In the following paragraphs, challenges associated with this approach are identified and then an alternative technique is described.

For discussion purposes, assume that an AFM probe can be modeled as a uniform cross-section cantilever beam with a force[4] applied at its free end (see Fig. 11) and that it is sufficient to describe its bending behavior using Euler–Bernoulli beam theory. The vertical deflection at any point along the beam, y, can then be written as a function of the force and position along the beam, x. Specifically, $y = (Fx^2/6EI)(3L - x)$, where E is the elastic modulus, I is the moment of inertia, and L is the beam length. The cantilever stiffness, $k(x)$, is the ratio of the force to the deflection and depends on the position along the beam as shown in Eq. (1). The sensitivity of the stiffness to x is shown in Eq. (2).

$$k(x) = \frac{6EI}{x^2(3L - x)} \tag{1}$$

$$\frac{\partial k}{\partial x} = \frac{6EI(3x^2 - 6Lx)}{(3Lx^2 - x^3)^2} \tag{2}$$

As noted previously, the cantilever deflection is typically determined optically by reflecting a small diameter laser beam off the back side of the cantilever onto a position sensitive photodetector (PSD); see Fig. 12. Changes in the deflection cause the reflected beam's position on the detector to vary. Combining the PSD output with the cantilever stiffness enables the force to be inferred. A stage (usually the AFM's own vertical scanner) that is capable of executing accurate displacements is often used to force the cantilever into contact with a rigid surface while monitoring the PSD output. In this way, the PSD output can be directly related to a known imposed deflection and the PSD voltage calibrated in terms of displacement. The point of contact between the cantilever and surface, however, can be ambiguous, particularly for tipless cantilevers like the one shown in Fig. 11. In some instances, the cantilever deflection is measured at a specific location using an instrument, such as a laser vibrometer or fiber interferometer, that can be focused to a small spot and provide an absolute displacement measurement at a specified point along the cantilever. However, it can be difficult to accurately identify the location of this point. In either case, the accuracy of subsequent force calculations can be degraded due to these positional uncertainties.

For example, assume that the stiffness is perfectly known for the force scenario shown in Fig. 11 with the deflection measured at the free end, $x = L$. According to Eq. (1), the stiffness is $k(L) = 3EI/L^3$. The corresponding sensitivity of stiffness to the actual measurement location (for small perturbations in x near $x = L$) is:

$$\left.\frac{\partial k}{\partial x}\right|_{x=L} = \frac{-9EI}{2L^4} = \left(\frac{3EI}{L^3}\right) \cdot \frac{-3}{2L} = k(L) \cdot \frac{-3}{2L}. \tag{3}$$

Consider a contact mode probe with a length $L = 200\,\mu m$ and loading conditions that match Fig. 11. According to Eq. (3), the ratio of the change in stiffness, Δk, to the calibrated stiffness for an error in contact location, which might occur during the displacement calibration procedure, (relative to $x = L$) of $\Delta x = -5\,\mu m$ is:

$$\frac{\Delta k}{k(L)} = \frac{-3}{2L}\Delta x = \frac{-3}{2 \cdot 200}(-5) = 0.038. \tag{4}$$

This represents a 3.8% error and imposes an upper bound on the accuracy. Note that this only considers the error due to contact location and assumes that the measured deflection is error free and the stiffness value at $x = L$ is exact. Neither of these conditions is true in general, further degrading measurement accuracy.

[4] This simple representation of the probe–surface interaction forces is for convenience only.

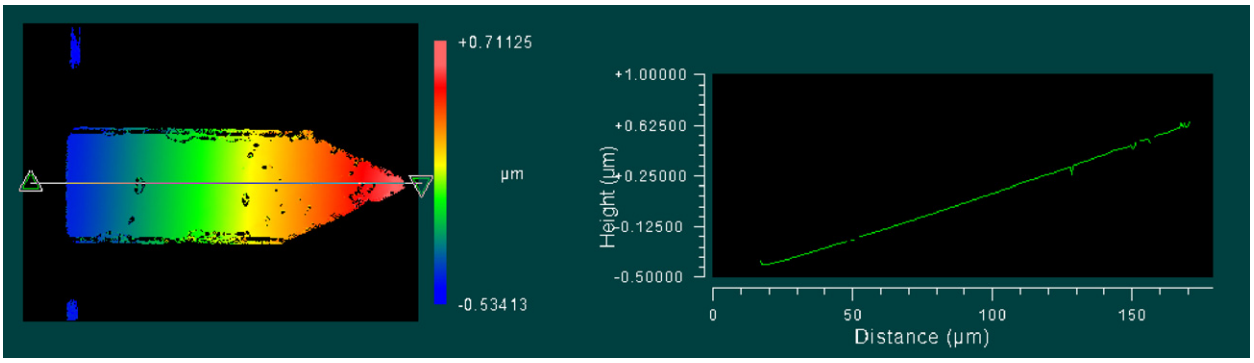

Fig. 10. This Olympus OMCL-AC160TS (42 N/m) cantilever shows a linear bending profile rather than the expected cubic behavior.

For tipped cantilevers, the uncertainty associated with the displacement calibration is usually negligible, although the effective cantilever length must be adjusted. In this case, it is important to recognize that the PSD signal depends on the cantilever slope, which is sensitive to the boundary conditions at the tip. Because a friction force is typically present between the tip and rigid surface (Fig. 13), the well-known hysteresis in the bi-directional displacement behavior is obtained.

The presence of the friction force highlights another limitation of the scalar $F = ky$ approach: the friction conditions during a measurement differ in general from the calibration conditions. Due to the friction force, F_f, a moment, $M = F_f \cdot d$, is present. The deflection due to this moment is $y = Mx^2/2EI$. By superposition, the total deflection due to both the moment and force F is then $y = (Fx^2(3L - x)/6EI) + (Mx^2/2EI)$. Writing F_f as μF, where μ is the friction coefficient between the tip and test surface, and substituting for M gives:

$$y = \frac{F((3L + 3\mu d)x^2 - x^3)}{6EI}. \tag{5}$$

The new cantilever stiffness is given in Eq. (6). The sensitivity of the stiffness to μ is shown in Eq. (7).

$$k(x) = \frac{6EI}{(3Lx^2 - x^3 + 3\mu dx^2)} \tag{6}$$

$$\frac{\partial k}{\partial \mu} = \frac{-18EIdx^2}{(3Lx^2 - x^3 + 3\mu dx^2)^2} \tag{7}$$

If the deflection is measured at the free end, $x = L$, the stiffness is $k(L) = 6EI/(2L^3 + 3\mu dL^2)$ and the corresponding sensitivity to the friction coefficient is:

$$\left.\frac{\partial k}{\partial \mu}\right|_{x=L} = \frac{-18EIdL^2}{(2L^3 + 3\mu dL^2)^2} = \frac{6EI}{(2L^3 + 3\mu dL^2)} \frac{-3dL^2}{(2L^3 + 3\mu dL^2)}$$

$$= k(L) \cdot \frac{-3dL^2}{(2L^3 + 3\mu dL^2)}. \tag{8}$$

Assume that the cantilever stiffness calibration was performed under the conditions shown in Fig. 13 with $\mu = 0.5$. For a tip distance of $d = 10\,\mu$m, the ratio of the change in stiffness to the nominal stiffness for a change in friction coefficient of $\Delta\mu = -0.3$ (due to a different test surface material, for example) is:

$$\frac{\Delta k}{k(L)} = \frac{-3dL^2}{(2L^3 + 3\mu dL^2)} \Delta\mu = \frac{-3(10)200^2}{(2 \cdot 200^3 + 3(0.5)(10)200^2)}(-0.3)$$

$$= 0.022. \tag{9}$$

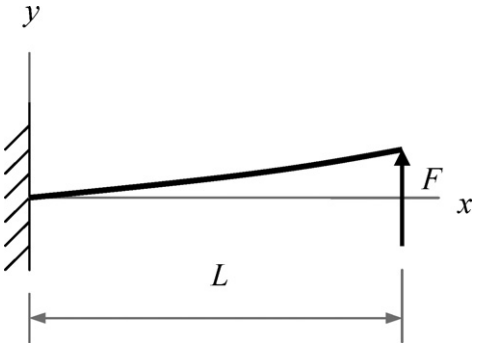

Fig. 11. Cantilever beam.

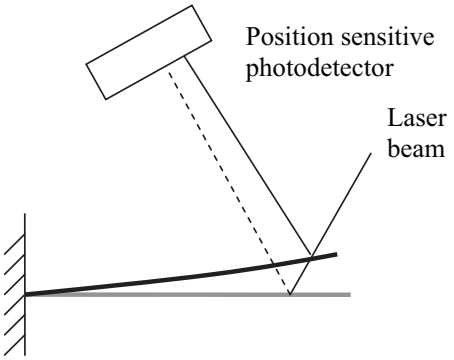

Fig. 12. Single point deflection measurement.

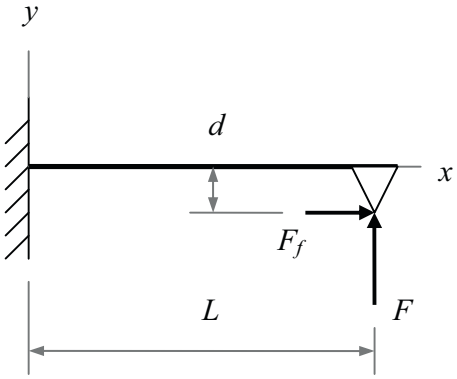

Fig. 13. Cantilever beam with friction force at the tip.

Again, this 2.2% error places an upper bound on the achievable accuracy. As before, this analysis only considers the error due to changes in friction coefficient between the tip and test surface and assumes that the measured deflection and calibrated stiffness value are error free. Additionally, it does not incorporate the error that would be obtained if the stiffness calibration was performed by a different method (e.g., vibration analysis or mass loading) such that the force conditions during calibration differed from the actual measurement situation.

The previous discussion highlights the limitations in single point deflection measurements for AFM force determination. An alternative to the traditional approaches for stiffness calibration that takes advantage of the deflection profile made available by the interferometric measurement platform is described next.

4.2. Full-field deflection measurement

Returning to the simple two-dimensional analysis shown in Fig. 11, assume that the full deflection profile, $y(x)$, for the cantilever is measured during loading. As shown in Eq. (5), the deflection can be described by a third order polynomial:

$$y(x) = 0 + 0x + \frac{F(3L + 3\mu d)}{6EI}x^2 - \frac{F}{6EI}x^3 = c_0 + c_1x + c_2x^2 + c_3x^3, \tag{10}$$

where the c_0 and c_1 coefficients are nominally zero. Given the full-field measurement, $y(x)$, the least-squares solution for the polynomial coefficients may be calculated. Using only these coefficients, the force and friction coefficient can then be uniquely determined by Eqs. (11) and (12).

$$F = -6c_3EI \tag{11}$$

$$\mu = \frac{-(3c_3L + c_2)}{3c_3d} \tag{12}$$

Eq. (11) is interesting because it requires little information about the beam. It applies regardless of the load application point, the beam stiffness, or the beam length. All that is necessary is a physical description of the beam's cross-section and the material properties (although obtaining these can sometimes still impose difficulties). Eq. (11) follows from the definition of shear, V, in an Euler–Bernoulli beam:

$$\frac{d^3y}{dx^3} = \frac{-V}{EI} = \frac{-F}{EI}, \tag{13}$$

which remains constant along the beam length for any boundary condition. By extension, the shear force in a beam of any shape can be determined from a multipoint measurement over a section of the beam as long as that section follows the assumptions that led to Eq. (11). This applies, for example, to triangular shaped beams since each leg may be considered to be an Euler–Bernoulli beam. The complete force vector can be determined using c_2 to find the friction force component, but this requires more information about the beam. This paper focuses on the application of Eq. (11) and leaves Eq. (12) for future research.

4.3. Experimental results for polynomial fit method

Eq. (11) was evaluated for the case of a mesoscale horizontal beam (no tip) with a vertical mass-based load applied (i.e., F was ideally the only force component). The beam was fabricated from a 50.8 mm diameter, double-sided polished ⟨1 1 1⟩ silicon wafer by diamond cutting at the flat. The design dimensions for the beam were 1 mm wide, 5 mm long, and 0.3 mm thick. After fabrication, the dimensions were measured using the SWLI. The average width was 0.941 mm and the length was 4.820 mm (the SWLI lateral resolution was 4.4 μm for a 5× objective at 0.5× zoom with a 640 × 480

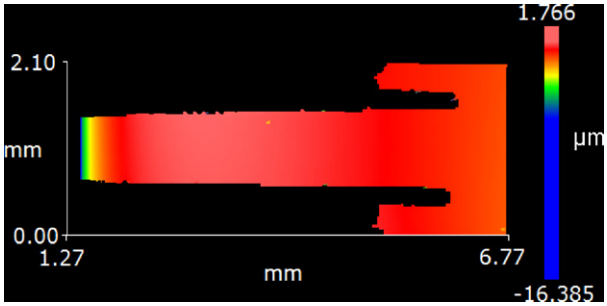

Fig. 14. SWLI image of the fabricated cantilever. The enlarged field of view was enabled by stitching multiple images together. It is seen that the width of the beam varies slightly along its length. The wafer edge roll-off is observed at the free end (left end) of the beam.

detector). A thickness measurement was completed by placing a glass surface beneath the cantilever and using the SWLI to measure the distance from the top of the glass surface to the top of the cantilever. The thickness value, t, was 0.305 mm (based on the system noise floor of 2.7 nm, the uncertainty in t is at least ±3 nm). A stitched SWLI image of the entire cantilever is shown in Fig. 14.

The vertical loads for the beam were produced using a series of 10 masses (Fig. 15); the individual masses were each suspended from a tether which was looped over the beam (Fig. 16). The mass values, m, were measured using a Mettler Toledo AB265-S/FACT precision balance (0.1 mg resolution). The beam was fixed to a holder using Crystalbond™ heat-activated adhesive and the holder was bolted to the tip-tilt stage.

The full-field measurement procedure was initiated by aligning the cantilever base to the SWLI optical axis (the optical axis was treated as parallel to the gravity vector, although the degree of alignment was not determined). To perform this alignment, a 5× objective with 0.5× zoom was applied to give a 2.82 mm by 2.12 mm field of view and 4.4 μm/pixel lateral resolution. The cantilever was then laterally positioned under the objective using the motorized stage. The cantilever was longer than the field of view so only a section of the cantilever was measured; stitching was

Fig. 15. Masses used for vertical loading experiments.

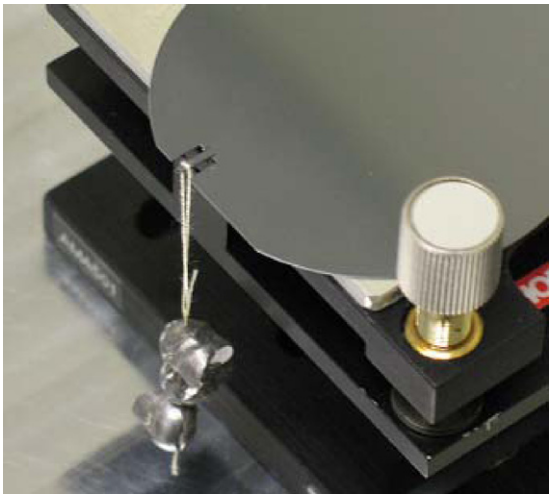

Fig. 16. The cantilever was attached to the tip-tilt stage and loaded near the free end. Measurements are valid at any section between the base and the load point.

not applied for the force measurements. The following steps were completed for each mass.

1. Attach the mass to the cantilever;
2. complete a first SWLI measurement;
3. remove the mass; and
4. complete a second SWLI measurement.

The two SWLI measurements were differenced to isolate the deflection caused by loading. As described before, differencing isolates the deformation caused by mass loading from other sources such as deformations caused by gravity loading. However, differencing requires lateral alignment between images. Therefore, the mass was applied first in the measurement sequence since it required the longest setup time. This reduced the time between step 2 and 4 to a few seconds, which mitigated the effect of lateral drift due to stage settling and thermal effects. In addition to drift-related lateral motion, vertical deflection of the cantilever from the mass loading also leads to a small shift (foreshortening) of the SWLI height map along the beam axis. Because the beam deflections were small in this study, this shear effect was neglected.

A deflection profile was obtained for each mass loading result by taking a section view through the beam center in the difference map. The data was then fit in a least-squares sense using a cubic polynomial to obtain the coefficient c_3. Eq. (11) was rearranged and F was replaced by mg ($g = 9.8\ \mathrm{m/s^2}$) to assist in the data analysis:

$$\frac{c_3}{m} = \frac{-9.8}{6E_{\langle 1\,1\,1\rangle} I} = C, \tag{14}$$

where the applied mass is expressed in grams, $E_{\langle 1\,1\,1\rangle} = 188$ GPa [33], $I = wt^3/12$ for the rectangular cross-section, $t = 0.305$ mm, and C is ideally a constant. There was a noticeable taper in the width, w, so the average value within the measurement field of view was used. Eq. (14) was evaluated as follows: (1) the left side was calculated using the measured values of c_3 and mass; (2) the right side was calculated based on the beam's physical description; and (3) the two values were compared. Ideally, they should agree within the measurement uncertainty. The uncertainty in c_3 was estimated based on 11 trials per each of the 10 weights. The standard deviation was multiplied by a coverage factor of 2. The results are displayed in Fig. 17. As seen in the figure, there is a small offset between the overall mean c_3/m value (left hand side of Eq. (14)) and the constant evaluated from the beam properties (right hand side of Eq. (14)). This difference is 0.4% and falls within the bounds set by the error bars.

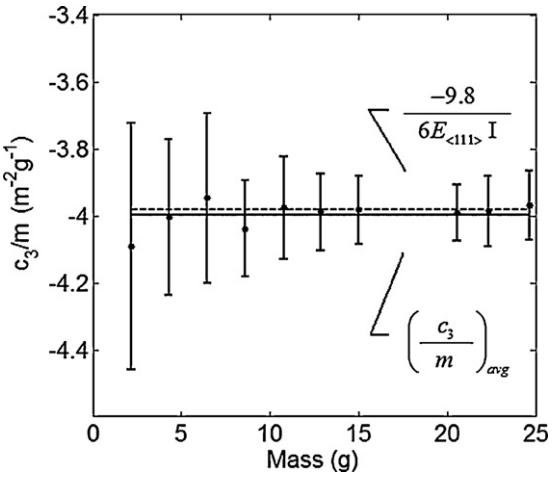

Fig. 17. Estimates of the Eq. (14) expressions for 10 masses. The error bars are based on a coverage factor of 2.

The variability of c_3 with profile location in a single measurement was also investigated. Eleven deflection profiles near the beam centerline were selected from a single image and used to individually calculate c_3. The standard deviation was found to be 0.5% of the mean value. This deviation is an indicator of the model limits since the Euler–Bernoulli equations describe a two-dimensional beam; non-ideal loading conditions which imposed a slight twist to the beam about its axis would cause the profile to vary with location, for example. Noise in the SWLI height map from the single measurement result would also contribute.

Next, the cantilever was loaded and 11 separate measurements were sequentially completed before removing the load. Only the centerline profile was extracted from each measurement and was used to calculate c_3. The standard deviation was found to be 1.5% of the mean. This provides an indication of the limit imposed by the environmental noise over the required measurement time of approximately 4 minutes.

Ideally, the force calculated using Eq. (11) is independent of the measurement location for constant loading conditions. To test this behavior, a measurement (denoted 1) was completed for a field of view near the free end and compared to a measurement (denoted 2) completed near the base; see Fig. 18. The values of c_3 differed, however, due to the variable beam width along its length (see Fig. 14). To enable a direct comparison of the two results, it was necessary to consider the non-constant beam width and corresponding variation in the moment of inertia along the beam's axis. This was accomplished using the average widths, w_{avg}, of the beam for the two selected fields of view. The result was evaluated by rearrang-

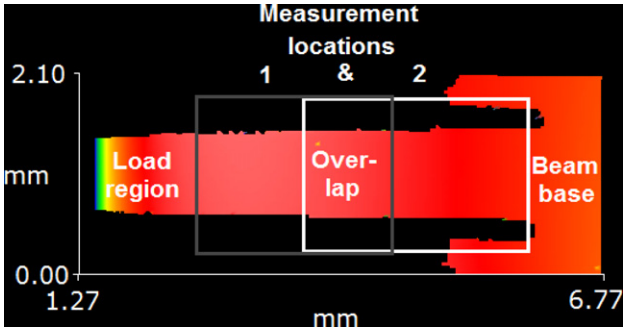

Fig. 18. A beam was loaded under identical conditions, but the measurement field of view was varied. The boxes represent the partially overlapping measurement regions along the beam's axis. For identical loading, the shear should be identical regardless of location.

ing Eq. (11), substituting for I, and considering the ratio of the two measurement results 1 and 2 (same mass, but different location). After simplification, the ratio is:

$$\frac{(-6c_3E_{\langle 1\,1\,1\rangle}I/mg)_1}{(-6c_3E_{\langle 1\,1\,1\rangle}I/mg)_2} = \frac{(-6c_3E_{\langle 1\,1\,1\rangle}w_{\text{avg}}t^3/12mg)_1}{(-6c_3E_{\langle 1\,1\,1\rangle}w_{\text{avg}}t^3/12mg)_2} = \frac{(c_3w_{\text{avg}})_1}{(c_3w_{\text{avg}})_2} = 1, \quad (15)$$

which is nominally equal to 1. Experimentally, the ratio was determined to be 1.03 based on the following values: $m = 8.617$ g, $(c_3)_1 = -37.02\ \text{m}^{-2}$, $(w_{\text{avg}})_1 = 0.88$ mm, $(c_3)_2 = -33.89\ \text{m}^{-2}$, and $(w_{\text{avg}})_2 = 0.93$ mm. This deviation from unity is reasonable given the 1.5% standard deviation obtained from the repeated c_3 tests for a single load with the profile extracted along the beam's centerline.

In a second study of the polynomial fit-based force determination approach, a horizontal Olympus OMCL-AC240TS probe (rectangular cross-section, 30 μm × 2.8 μm, 240 μm length, $k = 1.8$ N/m, ~14 μm tip height, less than 10 nm tip radius) was deflected vertically against a rigid, smooth silicon surface. The experimental c_3 value was $-2.11 \times 10^4\ \text{m}^{-2}$ from the centerline deflection profile. If the manufacturer-specified EI value of 8.29×10^{-12} N-m^2 is applied, the resulting vertical force is $F = -6c_3EI = -6(-2.11 \times 10^4)8.31 \times 10^{-12} = 1.05 \times 10^{-6}$ N = 1.05 μN. Based on the measured deflection of 0.59 μm at the probe's free end (from the SWLI height map), the force obtained from the manufacturer's spring constant is $F = 1.8(0.59 \times 10^{-6}) = 1.06 \times 10^{-6}$ N = 1.06 μN. This gives a 1% agreement and provides a preliminary validation of the method for a typical AFM probe. Data was collected using a 20× objective, 1x zoom, 320 × 240 pixel detector.

5. Conclusions

In this paper, an interferometric platform for measuring the full-field deflection of atomic force microscope (AFM) probes and generic cantilevers during quasi-static loading was presented. The platform consists of a scanning white light interferometer (SWLI), holders for the cantilevers, a translation stage, a rotation (tip-tilt) stage, and an adapter plate to connect these units to the SWLI table. Using the platform, studies were completed to enable visualization of cantilever behavior for snap-in against a rigid surface, cantilever-on-cantilever bending tests, and the anomalous bending profile for a damaged AFM probe. Additionally, the full-field deflection profiles measured by the platform were used to establish a new approach for normal force calculation. In this method, a polynomial fit to the cantilever deflection profile was used, in conjunction with the elastic modulus and area moment of inertia for the test beam, to estimate the normal force. Experimental validation was provided. Future efforts in this research will include: (1) expanding the analysis to a surface fit, rather than a line fit to the SWLI data as presented here; (2) extension of the approach to include the full, three-dimensional force vector at the probe tip; (3) completion of an uncertainty analysis; and (4) an evaluation of the effects of tip wear on measured force.

Acknowledgements

This work was partially supported by the National Institute of Standards and Technology. Any opinions, findings, and conclusions or recommendations expressed in this material are those of the authors and do not necessarily reflect the views of this agency.

References

[1] Binnig G, Quate CF, Gerber C. Atomic force microscope. Physical Review Letters 1986;56:930–3.
[2] Shenkenberg, D., Boldly going where no one has gone before, Photonics Spectra, December, 2008, pp. 68–71.
[3] Thundat T, Chen GY, Warmack RJ, Allison DP, Wachter EA. Vapor detection using resonating microcantilevers. Analytical Chemistry 1995;67/3:519–21.
[4] Vettiger P, Cross G, Despont M, Drechsler U, Durig U, Gotsmann B, et al. The "millipede"–nanotechnology entering data storage. IEEE Transactions on Nanotechnology 2002;1/1:39–55.
[5] Cumpson P, Zhdan P, Hedley J. Calibration of AFM cantilever stiffness: a microfabricated array of reflective springs. Ultramicroscopy 2004;100:241–51.
[6] Cleveland J, Manne S, Bocek D, Hansma P. A nondestructive method for determining the spring constant of cantilevers for scanning force microscopy. Review of Scientific Instruments 1993;64/7:1868–73.
[7] Butt HJ, Siedle P, Seifert K, Fendler K, Seeger T, Bamberg E, et al. Scan speed limit in atomic force microscopy. Journal of Microscopy 1993;169:75–84.
[8] Hutter J, Bechhoefer J. Calibration of atomic-force microscope tips. Review of Scientific Instruments 1993;64/7:1868–73.
[9] Li Y, Tao N, Pan J, Garcia A, Lindsay S. Direct measurement of interaction forces between colloidal particles using the scanning force microscope. Langmuir 1993;9/3:637–41.
[10] Neumeister JM, Ducker WA. Lateral, normal, and longitudinal spring constants of atomic force microscopy cantilevers. Review of Scientific Instruments 1994;65/8:2527–31.
[11] Senden T, Ducker W. Experimental determination of spring constants in atomic force microscopy. Langmuir 1994;10/4:1003–4.
[12] Smith S, Howard L. A precision, low-force balance and its application to atomic force microscope probe calibration. Review of Scientific Instruments 1994;65/4:903–9.
[13] Sader J, Larson I, Mulvaney P, White L. Method for the calibration of atomic force microscope cantilevers. Review of Scientific Instruments 1995;66/7:3789–98.
[14] Sader J. Parallel beam approximation for V-shaped atomic force microscope cantilevers. Review of Scientific Instruments 1995;66/9:4583–7.
[15] Gibson CT, Watson GS, Myhra S. Determination of the spring constants of probes for force microscopy/spectroscopy. Nanotechnology 1996;7:259–62.
[16] Myhra S. In: Riviere JC, Myhra S, editors. Handbook of Surface and Interface Analysis Methods for Problem Solving. New York: Marcel Dekker; 1998. p. 52.
[17] Sader J, Chon J, Mulvaney P. Calibration of rectangular atomic force microscope cantilevers. Review of Scientific Instruments 1999;70/10:3967–9.
[18] Levy R, Maaloum M. Measuring the spring constant of atomic force microscope cantilevers: thermal fluctuations and other methods. Nanotechnology 2002;13:33–7.
[19] Gibson C, Weeks B, Abell C, Rayment T, Myhra S. Calibration of AFM cantilever spring constants. Ultramicroscopy 2003;97:113–8.
[20] Ogletree D, Carpick R, Salmeron M. Calibration of frictional forces in atomic force microscopy. Review of Scientific Instruments 1996;67/9:3298–306.
[21] Bogdanovic G, Meurk A, Rutand MW. Tip friction–torsional spring constant determination. Colloids and Surfaces B: Biointerfaces 2000;19:397–405.
[22] Green CP, Lioe H, Cleveland JP, Proksch R, Mulvaney P, Sader JE. Normal and torsional spring constants of atomic force microscope cantilevers. Review of Scientific Instruments 2004;75/6:1988–96.
[23] Cannara R, Eglin M, Carpick R. Lateral force calibration in atomic force microscopy: a new lateral force calibration method and general guidelines for optimization. Review of Scientific Instruments 2006;77/5:053701.
[24] http://www.nist.gov/mel/mmd/mf/sfmet.cfm.
[25] Jabbour Z, Yaniv S. The kilogram and measurements of mass and force. Journal of Research of the National Institute of Standards and Technology 2001;106:25–46.
[26] Newell D, Kramar J, Pratt J, Smith D, Williams E. The NIST microforce realization and measurement project. IEEE Transactions of Instrumentation and Measurement 2003;4:158–61.
[27] Pratt J, Smith D, Newell D, Kramar J, Whitenton E. Progress toward Systèm International d'Unités traceable force metrology for nanomechanics. Journal of Materials Research 2004;19:1.
[28] Pratt J, Kramar J, Newell D, Smith D. Review of SI traceable force metrology for instrumented indentation and atomic force microscopy. Measurement Science and Technology 2005;16:2129–37.
[29] Gates R, Pratt J. Prototype cantilevers for SI-traceable nanonewton force calibration. Measurement Science and Technology 2006;17:2852–60.
[30] Pratt J, Kramar J, Shaw G, Smith D, Moreland J. A peizoresistive cantilever force sensor for direct AFM force calibration. Materials Research Society Symposium Proceedings 2007;1021:HH02–03.
[31] Langlois E, Shaw G, Kramar J, Pratt J, Hurley D. Spring constant calibration of atomic force microscopy cantilevers with a piezosensor transfer standard. Review of Scientific Instruments 2007;78:093705.
[32] Niehues J, Lehmann P, Bobey K. Dual-wavelength vertical scanning low-coherence interferometric microscope. Applied Optics 2007;46/29:7141–8.
[33] McSkimin H, Andreatch Jr P. Measurement of third-order moduli of silicon and germanium. Applied Physics 1964;35/11:3312–9.